



Universiteit  
Leiden  
The Netherlands

## Conductance and gating effects at sputtered oxide interfaces

Yin, C.

### Citation

Yin, C. (2019, July 3). *Conductance and gating effects at sputtered oxide interfaces*. *Casimir PhD Series*. Retrieved from <https://hdl.handle.net/1887/74527>

Version: Not Applicable (or Unknown)

License: [Leiden University Non-exclusive license](#)

Downloaded from: <https://hdl.handle.net/1887/74527>

**Note:** To cite this publication please use the final published version (if applicable).

Cover Page



Universiteit Leiden



The handle <http://hdl.handle.net/1887/74527> holds various files of this Leiden University dissertation.

**Author:** Yin, C.

**Title:** Conductance and gating effects at sputtered oxide interfaces

**Issue Date:** 2019-07-03

# 2

## **Experimental setups**

## 2.1. Thin film deposition

In the past few decades, progress in thin film deposition techniques has enabled material growth with unit cell precision, which has led to a large number of breakthroughs. Thin film deposition technologies are generally classified into two categories: physical vapor deposition (PVD) and chemical vapor deposition (CVD) [101]. The  $\text{LaAlO}_3/\text{SrTiO}_3$  interface is most commonly formed by pulsed laser deposition (PLD, PVD) [9], while several other growth methods, such as molecular beam epitaxy (MBE, PVD) [59], atomic layer deposition (ALD, CVD) [102] and sputtering (PVD) [57, 103], have also been employed. These alternative methods have not only demonstrated a successful growth of epitaxial  $\text{LaAlO}_3/\text{SrTiO}_3$  heterostructures, but also provide important experimental evidence for the emergence of interfacial conduction. A famous example is that Al-excess  $\text{LaAlO}_3$  films are necessary for forming conductive interfaces as could be demonstrated by MBE [59]. From an application point of view, amongst these methods, sputtering is the most extensively used technique in semiconductor industry. Therefore, fabricating  $\text{LaAlO}_3/\text{SrTiO}_3$  heterostructures by sputtering also facilitates its industrial application. In this thesis, we use a home-made  $90^\circ$  off-axis radio frequency magnetron sputtering system for growing  $\text{LaAlO}_3$  films. In this section, we first introduce the principles of sputter deposition and then discuss the main features of the  $90^\circ$  off-axis sputtering system.

### 2.1.1. Introduction to sputter deposition

The phenomenon of sputtering was discovered by Sir W. R. Grove in 1852 [104]. It was originally called "cathodic disintegration" which referred to the ejection of small particles. In 1913, Sir J. J. Thomson renamed cathodic disintegration to "spluttering" in his influential monograph [105]. In 1923, Kingdon and Langmuir removed the letter "l" from spluttering in their publication [106]. Ever since, the term "sputtering" has been used to describe cathodic disintegration of materials. The fundamentals of sputtering was already understood in early 20th century. However, sputtering actually played an important role in microelectronic industry since 1970s, because of the progress in sputtering source and vacuum technology.

Sputter deposition can be easily understood by considering a simple DC diode sputtering system, which consists of a cathode and an anode inside a vacuum chamber, as shown in Fig. 2.1(a). The cathode is the sputtering target and the substrate is placed on the anode, which is often at ground potential together with the vacuum chamber. After pumping the chamber to a base pressure (typically  $1 \times 10^{-6}$  mbar), a sputtering gas (usually Ar) is introduced into the chamber, reaching a pressure between  $1 \times 10^{-3}$  to  $1 \times 10^{-1}$  mbar. With a sufficient DC voltage applied between the electrodes, the gas will breakdown to form a plasma. The positively charged  $\text{Ar}^+$  ions are accelerated to-

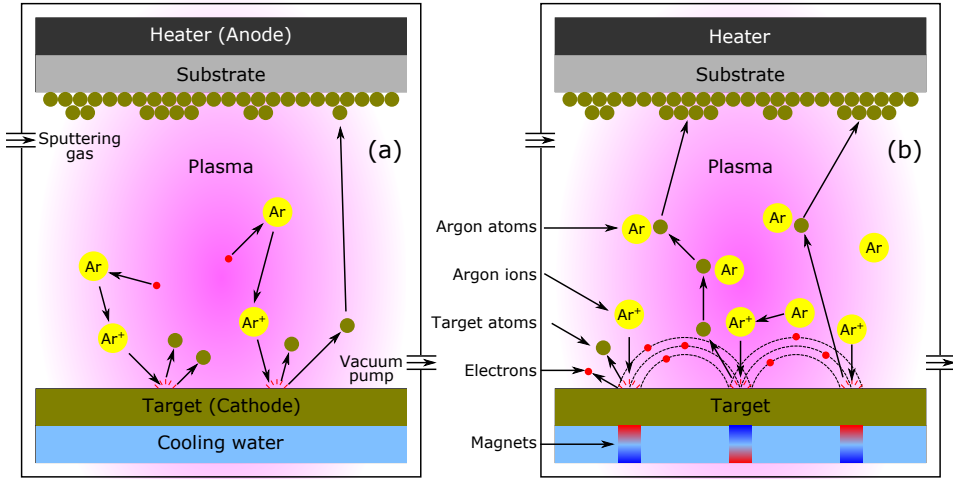


Figure 2.1: Principles of sputter deposition. (a) In a DC diode sputtering system, Ar atoms are ionized by a strong electric potential difference, and these ions are accelerated to the target. After impact, target atoms are released and travel to the substrate, where they form a thin film of the target material. (b) In a magnetron sputtering system, the electrons are confined near the target surface, which results in greater Ar ion replenishment and less damage of the substrate.

wards the negatively charged target to eject atoms from its surface. The ejected atoms then travel to the substrate and finally condense onto the substrate to form a thin film of the target material. DC sputtering can be operated only if the target is conductive. If the target is insulating, positive charges will build up at the target surface and repels the incident  $\text{Ar}^+$  ions. Consequently, the negative voltage on the target becomes lower than the breakdown voltage required to sustain the discharge.

The problem can be overcome by coupling a radio frequency (RF) voltage capacitively to the insulating target and the plasma. The commonly used frequency is 13.56 MHz. The electrons in the plasma oscillate with this high-frequency electric field, which results in two important effects. First, the positive surface charges are neutralized by the electrons in each RF cycle. Second, the electrons gain enough energy to make ionizing collisions to sustain the discharge. In contrast, the massive  $\text{Ar}^+$  ions in the plasma have too much inertia to follow 13.56 MHz and can only respond to the time-averaged electric field, which makes that the target self-biases to a negative potential. This bias, called DC bias, is generally related to the energy of the  $\text{Ar}^+$  ions hitting the target. In practice, an impedance matching network is required in order to transfer the RF power into the system more efficiently. The matching networks usually consist of capacitors and inductors. There are many different designs in the market but their sole purpose is to convert the impedance of the chamber to  $50\ \Omega$ .

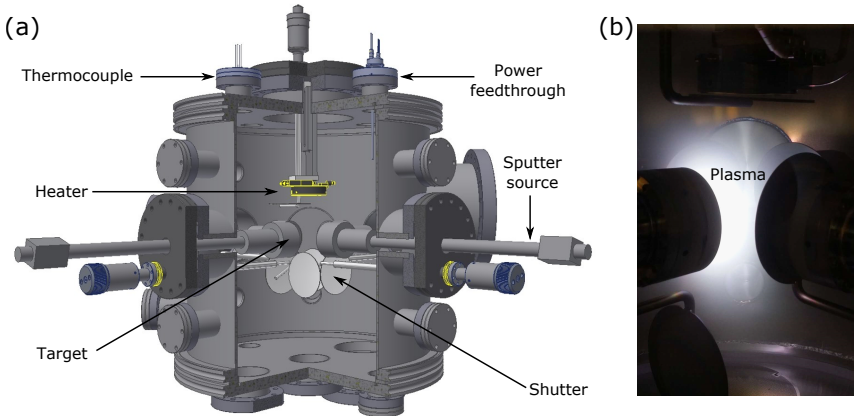


Figure 2.2: (a) A sketch of the  $90^\circ$  off-axis sputtering system. Image plotted by F. Schenkel. (b) A photo of the chamber taken during sputtering. The bright area is the plasma.

A common way to enhance the sputtering process is to use a magnetron sputtering source as shown in Fig. 2.1(b). The strong magnetic fields guide electrons to spiral along the magnetic flux lines near the target surface instead of being attracted toward the substrate. The enhanced confinement of electrons has two advantages. First, electrons travel for longer distances, increasing the probability of ionizing Ar atoms. Second, it prevents damages to the film caused by bombardment from the electrons.

### 2.1.2. $90^\circ$ off-axis sputtering

Conventional sputter deposition uses the on-axis geometry, where the substrate faces the target directly. However, when growing oxide films, backsputtering of the substrate by high-energy particles ( $O^-$  and sputtered atoms) usually degrades the quality of films. The problem can be solved by changing the relative position between the substrate and the target. The  $90^\circ$  off-axis geometry, where the substrate and the target are at a right angle, was first employed by Eom *et al.* [107, 108] for growing  $YBa_2Cu_3O_7$  thin films. This technique benefits both from off-axis geometry and high sputtering pressure. The idea is that the off-axis geometry places the substrate outside the plasma, and the sputtered atoms experience many scattering events with the sputtering gas to slow down before landing on the substrate. As a consequence, bombardments from high-energy particles are largely minimized.

A sketch of the  $90^\circ$  off-axis sputtering system in Leiden is shown in Figure 2.2(a). It is based on a system in use in the group of J.-M. Triscone in Geneva, who readily provided the technical details. A resistive heater (Twente Solid State Technology) is fixed on the central holder, and is grounded to the chamber. Four 2-inch magnetron sputtering

sources (MeiVac) are installed to the chamber wall at angles of  $90^\circ$ . Sputtering targets are glued to copper plates by epoxy adhesive silver. Magnetic keepers are screwed to the back of the copper plates and the targets are attached to the central magnet on the sputtering sources. The working distances are set at 75 mm from the surface of the heater to the axis of the target and 45 mm from the surface of the target to the axis of the heater. It should be noted that the working distances strongly affect the optimal growth parameters, especially the sputtering pressure. Three gas lines, namely Ar,  $O_2$  and  $N_2$  (Linde gas, purity  $\geq 99.999\%$ ), are connected to the chamber and the gas flows are measured by mass flow controllers (Brooks Instrument). The system is turbo-pumped and reaches a base pressure of  $1 \times 10^{-7}$  mbar. During sputtering, the chamber pressure is controlled by a butterfly valve (VAT) and the RF power is delivered to the sputtering source by Advanced Energy power supply (RFX-600) and matching networks (ATX-600). A photo of the chamber during sputtering is shown in Figure 2.2(b), where the heater is positioned well outside of the plasma.

## 2.2. Sample fabrication

### 2.2.1. Substrate Preparation

It was demonstrated in the original paper by Ohtomo and Hwang that a conductive interface can only be formed by growing  $LaAlO_3$  on  $TiO_2$ -terminated  $SrTiO_3$  [9]. The first step of our sample fabrication process is substrate preparation. The single crystalline  $SrTiO_3$  substrates used in this thesis are ordered from CrysTec GmbH. They are (001) oriented with dimensions of  $5 \times 5 \times 0.5$  mm<sup>3</sup> and miscut angles of  $0.1^\circ$ - $0.3^\circ$ .

The as-received substrate usually has a mixed surface termination of SrO and  $TiO_2$ . We follow the recipe established by Koster *et al.* [109] to obtain a pure  $TiO_2$  termination. The substrate is first ultrasonically cleaned in acetone, ethanol and isopropanol for 10 min, respectively, to remove dust. It is then soaked in millipore water ( $18.2$  M $\Omega$  cm at  $25^\circ$  C) in an ultrasonic bath for 30 min. This is an important step, during which the SrO-terminated areas form a Sr-hydroxide complex which is known to be dissolvable in acid, while the chemically stable  $TiO_2$ -terminated areas remain unaffected. To dissolve the Sr-hydroxide complex the substrate is etched in buffered HF ( $NH_4F:HF = 7:1$ , J. T. Baker) for 30 s. Finally, it is annealed in a quartz tube placed in a tube furnace (Lindberg/Blue) at  $980^\circ$  C for 1 h with an oxygen flow of 150 sccm to remove the residuals of the previous treatments and facilitate recrystallization.

Fig. 2.3(a) shows a typical atomic force microscopy image of a  $TiO_2$ -terminated  $SrTiO_3$  substrate. An atomically flat surface with step-and-terrace structures can be clearly seen. As shown in Fig. 2.3(b), the step height corresponds to the  $SrTiO_3$ (001) interplanar distance ( $\sim 3.91$  Å) and the terrace width is about 200 nm.

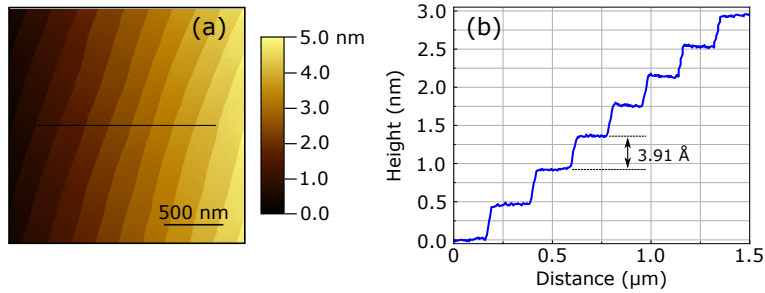


Figure 2.3: (a) A typical atomic force microscopy image of  $\text{TiO}_2$ -terminated  $\text{SrTiO}_3$  substrate. (b) A step-and-terrace profile. The step height is  $\sim 3.91 \text{ \AA}$  and the terrace width is about 200 nm.

### 2.2.2. Thin film growth

The substrate is first glued on the heater by uniformly applying a thin layer of silver paste (SPI Supplies) to the unpolished side. In order to get a good thermal contact and adhesion with the heater, the substrate is then baked at  $200^\circ\text{C}$  for 1 h in the chamber. Before deposition the chamber is usually pumped overnight.

When growing a film, the substrate is first heated up to the growth temperature at a rate of  $25^\circ\text{C}/\text{min}$ . Ar is then introduced into the chamber as the sputtering gas. Next, the target is pre-sputtered for at least 15 min while keeping the substrate shutter closed. After pre-sputtering, the deposition is started by opening the substrate shutter. The film thickness is controlled by varying the sputtering time. Since the film is grown in a reducing atmosphere, a post oxygen annealing treatment is necessary to remove the oxygen vacancies formed in the substrate. After deposition, the sample is cooled down to  $600^\circ\text{C}$  at a rate of  $10^\circ\text{C}/\text{min}$ , while the sputtering gas is pumped out at the same time. When the temperature stabilizes, oxygen is introduced into the chamber, reaching a pressure of 1 mbar. The annealing time is 1 h. After oxygen annealing, the sample is cooled down to room temperature in the same oxygen atmosphere and at the same cooling rate. The above steps describe the general film growth procedure. The optimization of growth parameters is discussed in more detail in Chapter 3.

### 2.2.3. Hall bar device fabrication

Besides unpatterned films, we also fabricated Hall bar devices using photolithography for electrostatic gating experiments. We use a Karl Suss Mask Aligner equipped with a 365 nm (i-line) ultraviolet (UV) lamp. A self-designed 5-inch chrome mask plate is ordered from Delta Mask, which contains Hall bar structures with different dimensions. The photoresist (OiR 907-12) and developer (OPD 4262) are from Fujifilm. A schematic of the device fabrication process is shown in Fig. 2.4.

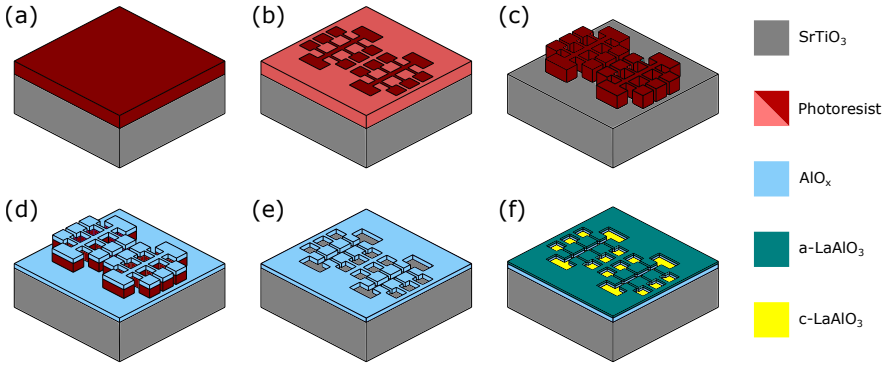


Figure 2.4: A schematic of the Hall bar device fabrication process. (a) Spin coating. (b) UV light exposure. (c) Photoresist development. (d)  $\text{AlO}_x$  film deposition. (e) Lift-off. (f)  $\text{LaAlO}_3$  film deposition.

First (Fig. 2.4(a)), the photoresist is spin coated (4000 rpm) on a  $\text{TiO}_2$ -terminated  $\text{SrTiO}_3$  substrate. The sample is then baked on a hot plate at  $80^\circ\text{C}$  for 1 min.

Second (Fig. 2.4(b)), the sample is exposed in UV light for 6 s. OiR 907-12 is a positive resist, therefore we cover the Hall bar pattern and expose the rest area.

Third (Fig. 2.4(c)), the sample is developed in OPD 4262 for 1 min, followed by dipping in a stop bath (millipore water) for 1 min. A Hall bar structure made of photoresist is now formed on the substrate.

Fourth (Fig. 2.4(d)), an amorphous  $\text{AlO}_x$  layer ( $\sim 15$  nm) is sputtered (DC bias set to  $-750$  V) on the sample by a Leybold-Heraeus sputtering system. In order to prevent hardening of the photoresist, we alternate the sputtering on and off in every 1 min, which is achieved by rotating the sputtering source back and forth with a motor.

Fifth (Fig. 2.4(e)), the sample is soaked in acetone overnight to lift-off the photoresist. The sample is then ultrasonicated in acetone and isopropanol, both for 5 min. The substrate is now covered by an  $\text{AlO}_x$  hard mask except for the Hall bar pattern.

Finally (Fig. 2.4(f)), the  $\text{LaAlO}_3$  film is grown by the process mentioned above. The  $\text{LaAlO}_3$  layer formed on the Hall bar pattern is crystalline and conductive while the layer formed on  $\text{AlO}_x$  is amorphous and insulating.

It is worth mentioning that after step 5, there is usually some residual photoresist left on the Hall bar pattern as shown in Fig. 2.5(a). The problem cannot be solved by lowering the DC bias or extending the soaking time in acetone. However, the residual photoresist can be cleaned away during heating up the substrate to the growth temperature as shown in Fig. 2.5(b). We have also tried to fabricate Hall bar devices in the same procedure but using e-beam lithography (PMMA from Allresist). However, we usually find more residual resist on the Hall bar pattern, which cannot be removed by heating up the substrate to high temperatures.

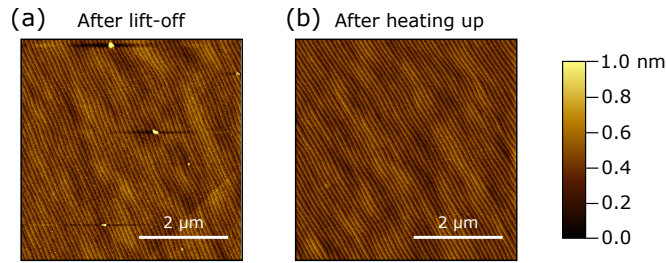


Figure 2.5: (a) An AFM image of the Hall bar channel after lift-off. Residual photoresist is clearly visible. (b) An AFM image taken after heating up the substrate to 800 °C. Residual resist is cleaned away during the heating up process.

## 2.3. Sample characterization

The main disadvantage of our sputtering system is that it lacks *in situ* tools such as reflection high-energy electron diffraction (RHEED) or a quartz crystal monitor to check the growth process. Therefore, we rely on *ex situ* characterization techniques, such as atomic force microscopy and x-ray diffraction, to determine the thickness and lattice constants of the  $\text{LaAlO}_3$  films.

### 2.3.1. Atomic force microscopy

Atomic force microscopy (AFM) is a type of scanning probe microscopy (SPM), which was invented by Binnig *et al.* [110] in 1986. It is one of the foremost techniques for characterizing surface topography with nanometer resolution. AFM is based on measuring the repulsive and attractive forces between atoms on the probe and those on the sample surface. Therefore it enables measurements on insulating materials. An AFM basically consists of a laser, a four-sectional photodiode and a piezoelectric scanner. In the measurement, a spring microcantilever with a sharp tip (typical radius less than 10 nm) scans over the sample surface in a raster-like pattern. As the tip interacts with the sample surface, the laser spot is reflected from the cantilever and detected by the photodiode. In order to maintain feedback parameters constant, a feedback loop uses the laser deflection to adjust the height of the cantilever, forming the surface topology. We use a Bruker AFM and choose its tapping mode, where the topology is mapped by an oscillating tip lightly tapping the sample surface.

### 2.3.2. X-ray diffraction

High resolution x-ray diffraction (HRXRD) is a powerful tool for nondestructive investigations of thin films, heterostructures and superlattices. The high resolution is achieved by using combinations of high quality mirror and monochromator. We use a Bruker XRD

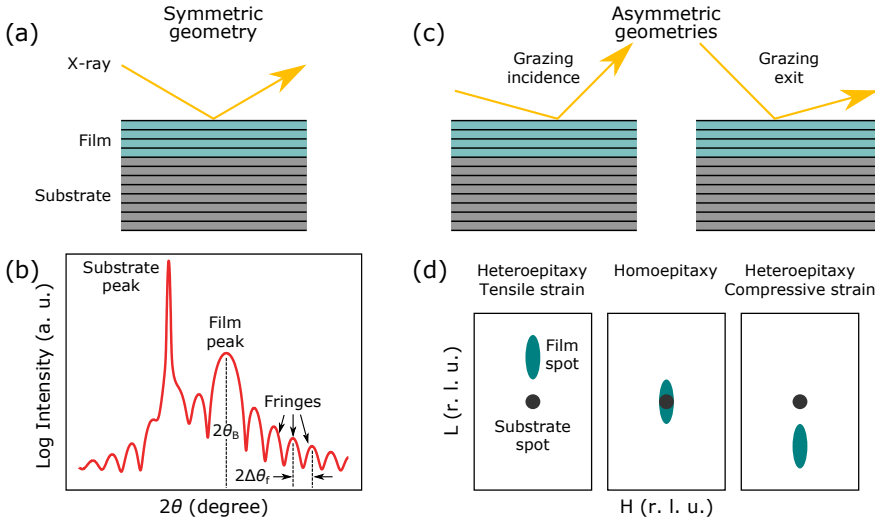


Figure 2.6: Schematics of high resolution x-ray diffraction. (a) A sketch of the symmetric geometry. (b) A canonical result of a  $\theta$ - $2\theta$  scan. The film peak appears at  $2\theta_B$  and the difference between interference fringes is  $2\Delta\theta_f$ . Image adapted from open source. (c) Sketches of the asymmetric geometries. (d) Canonical results of reciprocal space mapping. The map is in reciprocal lattice units (r. l. u.) based on the principal Bragg indices  $H$ ,  $K$  and  $L$ . In the geometry used,  $(HOL)$  spots are measured. The relative position between the substrate spot (black) and film spot (teal) depends on the epitaxial strain on the film.

(D8 DISCOVER) which is equipped with a Cu  $K_{\alpha 1}$  ( $\lambda = 1.541 \text{ \AA}$ ) monochromator in the incident beam optics and a motorized receiving slit in the diffracted beam optics. This equipment was kindly made available by A. Caviglia at Delft University of Technology. The routine measurements include  $\theta$ - $2\theta$  scans and reciprocal space mapping, which allow for the precise measurement of film thickness and lattice constants.

The  $\theta$ - $2\theta$  scan is performed in a symmetric geometry as shown in Fig. 2.6(a). A canonical result is plotted in Fig. 2.6(b). The film peak appears at  $2\theta_B$ . The lattice constant perpendicular to the surface,  $d$  (also called the out-of-plane lattice constant), can be obtained from the Bragg equation,

$$2d \sin\theta_B = n\lambda, \quad (2.1)$$

where  $n$  (integers) is the diffraction order and  $\lambda$  is the x-ray wavelength. Moreover, interference fringes are usually observed next to the main diffraction peak. The angular difference between such secondary maxima,  $\Delta\theta_f$ , can be used to determine the film thickness [111],

$$t = \frac{\lambda}{2\Delta\theta_f \cos\theta_B}, \quad (2.2)$$

where  $\Delta\theta_f$  is in rad.

Reciprocal space mapping (RSM) is performed in an asymmetric geometry, which allows for the determination of both the in-plane ( $a_{\text{film}}$ ) and out-of-plane ( $c_{\text{film}}$ ) lattice constants. There are two asymmetric geometries, namely grazing incidence (GI) and grazing exit (GE) as shown in Fig. 2.6(c). We use the GI geometry, since it is more surface sensitive compared with the GE geometry. It is known that a lattice plane in real space corresponds to a point in reciprocal space. Typical RSM results around the ( $H0L$ ) diffraction peak are plotted in Fig. 2.6(d). The black and teal spots represent the substrate and film peaks, respectively. The elongation of the film spot is due to finite thickness effects. In all of the three cases, the film is fully strained to the substrate, with equal values of  $H$  for both. However, the relative position between the substrate and film spots for the out-of-plane component depends on the epitaxial strain on the film through the Poisson's ratio which is a measure of the Poisson effect. The Poisson effect is a phenomenon in which a material tends to contract in the directions perpendicular to the direction of stretching, and vice versa. When  $a_{\text{film}} = a_{\text{sub}}$ , the substrate and film spots overlap with each other. When  $a_{\text{film}} < a_{\text{sub}}$  ( $a_{\text{film}} > a_{\text{sub}}$ ), the film experiences a tensile (compressive) strain from the substrate. The film spot will appear above (below) the substrate spot. The lattice constants can be calculated by

$$\frac{a_{\text{sub}} - a_{\text{film}}}{a_{\text{sub}}} = \frac{\Delta H}{H} \quad \text{and} \quad \frac{c_{\text{sub}} - c_{\text{film}}}{c_{\text{sub}}} = \frac{\Delta L}{L} \quad (2.3)$$

### 2.3.3. Magnetotransport measurements

Magnetotransport properties of the  $\text{LaAlO}_3/\text{SrTiO}_3$  interface are the main focus of this thesis. Two cryostats are used for the measurements. One is a Quantum Design Physical Property Measurement System (PPMS), which controls magnetic fields up to 9 T and temperatures ranging from 1.9 K to 400 K. The other cryostat is in the high field magnet laboratory (HFML) of Radboud University Nijmegen, which is equipped with a 15 T superconducting magnet. Two temperatures can be easily stabilized in the Nijmegen cryostat, namely 4.2 K (pump valve fully closed) and 1.2 K (pump valve fully open).

#### Van der Pauw method

We use the van der Pauw method to measure unpatterned samples. This method was suggested by L. J. van der Pauw in 1958 [112, 113]. As shown in Fig. 2.7(a), four ohmic contacts 1, 2, 3, and 4 are formed at the corners by wedge bonding aluminum wire directly to the sample surface. We also make four scratches using a diamond knife to minimize errors arising due to the finite extent of contacts.

To measure the sheet resistance  $R_s$  (also called the longitudinal resistance  $R_{xx}$ ), a current is applied along one edge (for example,  $I_{12}$ ) of the sample and the voltage across the opposite edge (in this case,  $V_{43}$ ) is measured. The resistance along the vertical edge,

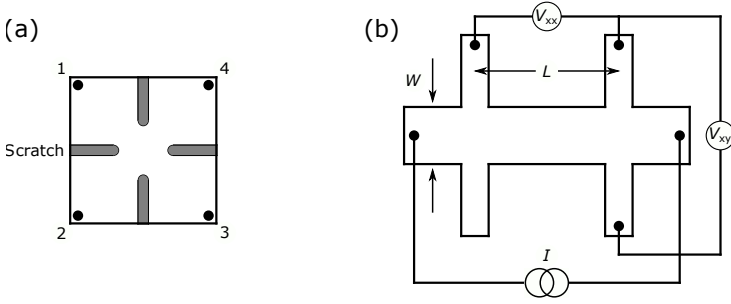


Figure 2.7: Sample geometries for magnetotransport measurement. (a) Van der Pauw method. (b) Hall bar geometry.

$R_{12,43}$ , can be obtained using Ohm's law,  $R_{12,43} = V_{43}/I_{12}$ . In a similar way, we can obtain a resistance along the horizontal edge, such as  $R_{23,14}$ . These two resistances are related to  $R_s$  by the van der Pauw formula

$$e^{-\frac{\pi R_{12,43}}{R_s}} + e^{-\frac{\pi R_{23,14}}{R_s}} = 1. \quad (2.4)$$

In practice, a more accurate measurement can be performed by exchanging the current source and voltage meter as well as switching their polarities. The vertical and horizontal resistances are then given by

$$R_v = \frac{R_{12,43} + R_{21,34} + R_{34,21} + R_{43,12}}{4} \quad \text{and} \quad R_h = \frac{R_{23,14} + R_{32,41} + R_{14,23} + R_{41,32}}{4}. \quad (2.5)$$

We use a fast-converging Newton-Raphson method to obtain  $R_s$ , where the next approximation  $R_s^+$  is calculated by

$$R_s^+ = R_s + R_s^2 \frac{1 - e^{-\frac{\pi R_v}{R_s}} - e^{-\frac{\pi R_h}{R_s}}}{\pi(R_v e^{-\frac{\pi R_v}{R_s}} + R_h e^{-\frac{\pi R_h}{R_s}})}. \quad (2.6)$$

The calculation converges when  $(R_s^+ - R_s)/R_s$  is less than the tolerable error (0.01 % in our calculation).

To measure the Hall resistance  $R_{\text{Hall}}$  (also called the transverse resistance  $R_{xy}$ ), a magnetic field is applied normal to the sample surface. The applied current, the measured voltage and the magnetic field must be perpendicular to each other. For instance, a current is driven from 1 to 3, and the voltage between 2 and 4 is measured. Two sets of measurements need to be made: one with the magnetic field in the positive (P)  $z$ -direction and the other in the negative (N)  $z$ -direction. Combining all the measurement configurations,  $R_{\text{Hall}}$  is given by

$$R_{\text{Hall}} = \frac{(R_{13,24,P} - R_{13,24,N}) + (R_{31,42,P} - R_{31,42,N}) + (R_{24,31,P} - R_{24,31,N}) + (R_{42,13,P} - R_{42,13,N})}{8}. \quad (2.7)$$

### Hall bar geometry

For a Hall bar geometry as shown in Fig. 2.7(b), the measurement and calculation are much easier. An electrical current,  $I$ , is applied along the Hall bar channel. The longitudinal voltage,  $V_{xx}$ , and transverse voltage,  $V_{xy}$ , can be measured simultaneously. The sheet resistance is given by

$$R_s = \frac{V_{xx}}{I} \frac{W}{L}, \quad (2.8)$$

where  $W$  is the Hall bar width and  $L$  is the distance between two voltage probes. The Hall resistance is given by

$$R_{\text{Hall}} = \frac{V_{xy}}{I}. \quad (2.9)$$

### Determination of carrier density and mobility

The carrier density ( $n_s$ ) and mobility ( $\mu$ ) of the sample are determined from magnetotransport measurements. It is well known that the 2DES at the  $\text{LaAlO}_3/\text{SrTiO}_3$  interface changes from one-band conduction to two-band conduction after a Lifshitz transition [63], which corresponds to the Hall resistance changing from linear to nonlinear<sup>1</sup>.

In the one-band regime,  $n_s$  and  $\mu$  are given by [115]

$$n_s = \frac{B}{eR_{\text{Hall}}} \quad \text{and} \quad \mu = \frac{R_{\text{Hall}}}{BR_s(B=0)}, \quad (2.10)$$

where  $e$  is the electron charge and  $B$  is the magnetic field.

In the two-band regime, the carrier densities and mobilities can be extracted by fitting the magnetotransport data with a two-band model [115]

$$R_s = \frac{1}{e} \cdot \frac{\frac{n_1\mu_1}{1+(\mu_1B)^2} + \frac{n_2\mu_2}{1+(\mu_2B)^2}}{\left(\frac{n_1\mu_1}{1+(\mu_1B)^2} + \frac{n_2\mu_2}{1+(\mu_2B)^2}\right)^2 + \left(\frac{n_1\mu_1^2B}{1+(\mu_1B)^2} + \frac{n_2\mu_2^2B}{1+(\mu_2B)^2}\right)^2} \quad (2.11)$$

and

$$R_{\text{Hall}} = \frac{1}{e} \cdot \frac{\frac{n_1\mu_1^2B}{1+(\mu_1B)^2} + \frac{n_2\mu_2^2B}{1+(\mu_2B)^2}}{\left(\frac{n_1\mu_1}{1+(\mu_1B)^2} + \frac{n_2\mu_2}{1+(\mu_2B)^2}\right)^2 + \left(\frac{n_1\mu_1^2B}{1+(\mu_1B)^2} + \frac{n_2\mu_2^2B}{1+(\mu_2B)^2}\right)^2}, \quad (2.12)$$

where  $n_{1(2)}$  and  $\mu_{1(2)}$  are the carrier density and mobility of the first (second) band, respectively.

<sup>1</sup>It should be noted that a nonlinear Hall resistance can also arise due to anomalous Hall effect [114].